



Published in final edited form as:

*IEEE Trans Med Imaging*. 2012 May ; 31(5): 1043–1050. doi:10.1109/TMI.2012.2184551.

## An Efficient Interlaced Multi-shell Sampling Scheme for Reconstruction of Diffusion Propagators

**Wenxing Ye**[Student Member, IEEE]

Department of Computer and Information Science and Engineering, University of Florida, Gainesville, FL, 32611, USA wye@cise.ufl.edu

**Sharon Portnoy**

Department of Neuroscience, McKnight Brain Institute, University of Florida, Gainesville, FL, 32611, USA sharon.portnoy@mbi.ufl.edu

**Alireza Entezari**\*[Member, IEEE]

Department of Computer and Information Science and Engineering, University of Florida, Gainesville, FL, 32611, USA

**Stephen J. Blackband**

Department of Neuroscience, McKnight Brain Institute, University of Florida, Gainesville, FL, 32611, USA blackie@mbi.ufl.edu

**Baba C. Vemuri**[Fellow, IEEE]

Department of Computer and Information Science and Engineering, University of Florida, Gainesville, FL, 32611, USA vemuri@cise.ufl.edu

### Abstract

In this paper, we propose an interlaced multi-shell sampling scheme for the reconstruction of the diffusion propagator from diffusion weighted magnetic resonance imaging (DWMRI). In standard multi-shell sampling schemes, sample points are uniformly distributed on several spherical shells in  $\mathbf{q}$ -space. The distribution of sample points is the same for all shells, and is determined by the vertices of a selected polyhedron. We propose a more efficient interlaced scheme where sample points are different on alternating shells and are determined by the vertices of a pair of dual polyhedra. Since it samples more directions than the standard scheme, this method offers increased angular discrimination. Another contribution of this work is the application of optimal sampling lattices to  $\mathbf{q}$ -space data acquisition and the proposal of a model-free reconstruction algorithm, which uses the lattice dependent **sinc** interpolation function. It is shown that under this reconstruction framework, the Body Centered Cubic (BCC) lattice provides increased accuracy. The sampling scheme and the reconstruction algorithms were evaluated on simulated data as well as rat brain data collected on a **600 MHz (14.1 Tesla)** Bruker imaging spectrometer.

### Keywords

Optimal Sampling Lattices; Diffusion Propagator; DW-MRI; Multi-shell; Interlaced Sampling

### I. Introduction

Diffusion MRI is a non-invasive imaging technique, which is sensitive to the Brownian motion of water molecules through tissue in vivo. Water molecules exhibit anisotropic

---

\*Corresponding Author entezari@cise.ufl.edu.

diffusion through a tissue that is rich in white matter fibers, with greater diffusion occurring along, rather than across, fibers. This directional preference allows one to infer connectivity patterns and monitor their changes over time, which has various clinical applications [1]

One of the major tasks in the field of diffusion MRI is the reconstruction of the 3-D diffusion propagator,  $P(\mathbf{r})$ , which characterizes the diffusion of water molecules in fibrous tissues with a probability density function (PDF). By integrating  $P(\mathbf{r})$  from  $\|\mathbf{r}\| = 0$  to  $\infty$ , the diffusion's orientation distribution function (ODF) is obtained and has been exploited by many recent developments as a replacement to  $P(\mathbf{r})$  [2], [3]. However, an ODF only provides the averaged angular information about the diffusion process. In contrast, the diffusion propagator,  $P(\mathbf{r})$ , provides both radial and angular information and describes the diffusion process more accurately. Because of the additional radial information,  $P(\mathbf{r})$  can be used to estimate extra features such as probability of diffusion permeability of the walls, average cell size, axonal diameter and other features that are useful in sensing white matter anomalies [4].

Under the narrow pulse assumption (i.e., the duration of the applied diffusion sensitizing gradients  $\delta$  is much smaller than the time between the two pulses),  $\Delta$ , the diffusion signal  $E(\mathbf{q})$  in  $\mathbf{q}$ -space and the diffusion propagator  $P(\mathbf{r})$  in displacement space are related through the Fourier transform [5]:

$$P(\mathbf{r}) = \int E(\mathbf{q}) \exp(-2\pi i \mathbf{q} \cdot \mathbf{r}) d\mathbf{q} \quad (1)$$

where  $E(\mathbf{q}) = S(\mathbf{q})/S_0$ ,  $S_0$  is the diffusion signal with zero diffusion gradient ( $\mathbf{q} = 0$ ),  $\mathbf{r}$  is the displacement vector,  $\mathbf{q} = \gamma\delta\mathbf{G}/2\pi$  is the reciprocal space vector,  $\gamma$  is the gyromagnetic ratio and  $\mathbf{G}$  is the gradient vector.

Several techniques have been proposed to reconstruct the diffusion propagator from the diffusion signal. Most of them assume a model for the  $E(\mathbf{q})$  and calculate  $P(\mathbf{r})$  through Fourier transform [6], [7].

Diffusion tensor imaging (DTI) proposed by [8] is a simple yet commonly used technique. It assumes that the diffusion signal can be modeled with an oriented Gaussian probability density function whose covariance matrix is a second-order symmetric positive definite tensor. For DTI, the estimation of this tensor is simple, the sampling burden is light. However, it is now well known that this model fails to capture complex fiber geometries within a voxel. This has led to several improved acquisition techniques and reconstruction methods [6], [7], [3], [9], [10], [11].

High angular resolution diffusion imaging (HARDI) was introduced to overcome the limitations of DTI through sampling many diffusion orientations, usually many more than needed by DTI. Several techniques have been proposed for the analysis of HARDI datasets that involve representing the diffusivity function by spherical harmonic expansion [12], [13], generalization of DTI using higher order tensors [14], [9], combining hindered and restricted models of water diffusion (CHARMED) [15], direct estimation of the fiber orientation using spherical deconvolution [16], a tensor distribution model introduced in [6], and the Diffusion Orientation Transform (DOT) [10].

Recently, reconstruction methods that employ multi-shell acquisitions in the  $\mathbf{q}$ -space have been investigated. Using multi-shell data, a diffusion-propagator reconstruction technique, based on Laplace equation, was introduced in [7]. In addition, a more accurate model for ODF reconstruction from multi-shell  $\mathbf{q}$ -ball imaging (QBI) data, was introduced in [3].

To varying degrees, most of these techniques assume that the diffusion signal obeys a particular model. Introducing a model, at times, offers the advantages of analytical reconstruction through Fourier transformation, smooth results which are resistant to noise, and a limited number of required samples. However, any model-based technique is inherently biased, as it will always produce results that obey the underlying model. This model bias on the diffusion signal will transfer to the reconstruction error of diffusion propagator through the Fourier transform.

A commonly-used approach decomposes  $E(\mathbf{q})$  into spherical and radial functions, each of which can be expanded in independent basis [7], [17], [18]. Often spherical harmonic basis are used to represent the spherical component of  $E(\mathbf{q})$  and different choices have been made for representing the radial component.

As an alternative to these methods, diffusion spectrum imaging (DSI), i.e.  $\mathbf{q}$ -space imaging (QSI) was proposed, which requires sampling the diffusion signal on a dense 3-D Cartesian lattice. The diffusion propagator can then be reconstructed using the 3-D Fast Fourier Transform (FFT). Refinements to this technique have included the use of alternative sampling lattices, such as the Body Centered Cubic (BCC) lattice [19], as well as the application of tomographic reconstruction principles [20]. DSI methods have weak assumptions about the diffusion signal and can be evaluated precisely through the Shannon sampling theorem. But the heavy sampling burden makes the acquisition time-intensive and limits their widespread application. Hybrid diffusion imaging (HYDI) [21] was proposed as an alternative to DSI. It samples diffusion signal on several spherical shells and estimates the signal values on a dense 3-D Cartesian lattice through linear interpolation. The idea of interpolating spherical samples onto a dense regular lattice is also used in our proposed method. However, HYDI acquires more samples on shells with higher  $b$ -values (similar to CHARMED [22]), where SNR decreases which leads to a less accurate reconstruction [23].

In this paper, we propose a novel approach for data acquisition and reconstruction of the diffusion propagator at each voxel. The approach was inspired by the work of [20] which exploits the Fourier transform relationship between  $P(\mathbf{r})$  and  $E(\mathbf{q})$  to develop a tomographic reconstruction of the propagator. By interpolating a relatively small number of samples of the  $\mathbf{q}$ -space diffusion signal onto a regular grid, their approach allows for a tomographic reconstruction of  $P(\mathbf{r})$  using the Fourier transform. Once  $E(\mathbf{q})$  is sampled on a regular lattice, its Fourier transform,  $P(\mathbf{r})$ , is replicated on the dual lattice. Each replica is then contained in a polyhedral voxel determined by the geometry of the dual lattice. Since  $P(\mathbf{r})$ , at each voxel (tile), may contain anisotropic features in *any* arbitrary direction, it behooves us to choose a tiling of the space where each tile captures the maximum radial content of  $P(\mathbf{r})$ . Optimal tiling of space results in voxels that admit a larger inscribing sphere compared to the traditional Cartesian tiling with cubic voxels.

The first contribution of this paper is the optimal  $\mathbf{q}$ -space discretization, such that each voxel in the displacement space (representing  $P(\mathbf{r})$  locally) is a rhombic dodecahedron and admits a larger inscribing sphere compared to the usual cubic voxels. This improvement in the reconstruction accuracy of  $P(\mathbf{r})$  is accomplished while the sampling density (and hence the acquisition time) remains the *same* as the cubic Cartesian tiling. The rhombic dodecahedral tile centers form a Face Centered Cubic (FCC) lattice, which is the densest sphere packing lattice in 3-D. As we will see in Section II, an FCC lattice in displacement space is achieved by discretizing the  $\mathbf{q}$ -space on a BCC lattice. Such a discretization leads to a more accurate reconstruction of the diffusion propagator as the ghosting effects are minimized.

The second contribution of this paper is the novel multi-shell sampling scheme. Unlike standard schemes, which have the same directional distribution of samples on each shell,

this “interlaced” scheme uses a pair of dual polyhedra, the icosidodecahedron and rhombic triacontahedron, to determine the sample distributions on odd and even shells, respectively. Since shells with larger radii demand higher sampling rates, one may consider distributing a larger number of samples on these shells corresponding to large  $b$ -values. However, at large  $b$ -values SNR is known to decrease [23], leading to a less accurate reconstruction. Our interlaced approach maintains the same number of sample points through all shells. We show that the interlaced scheme provides greater reconstruction accuracy, even with fewer total number of samples.

The rest of the paper is organized as follows: in Section II, we briefly introduce the notion of non-Cartesian lattice that will be used for representation of  $E(\mathbf{q})$  and reconstruction of  $P(\mathbf{r})$  discussed in Section IV. In Section III, we introduce the proposed interlaced sampling scheme and Section V contains experiments for comparing interlaced sampling to the standard multi-shell sampling scheme. Finally we present conclusions in Section VI.

## II. Multi-dimensional Lattices for Representation

A point lattice is a discrete subgroup of the Euclidean space that contains the origin. The **Voronoi cell** of a lattice point is formed by all the Euclidean points for which that lattice point is the closest one compared with all the other lattice points.

Points on a lattice are generated by integer linear combination of a set of vectors which are the columns of a sampling matrix,  $\mathbf{L}$ . Sampling a multi-dimensional signal on a lattice,  $\mathbf{L}$ , results in a periodic replication of its spectrum on the **reciprocal** lattice  $\widehat{\mathbf{L}}=\mathbf{L}^{-T}$ . The Voronoi cell of the reciprocal lattice is called a **Brillouin zone** [24] which is the unit cell for the periodic replication. If the periodicity of replication is large enough so that the replicas do not overlap with the main spectrum in the Brillouin zone, the original signal can be precisely reconstructed from the samples [25]. The boundary of the Brillouin zone is the multi-dimensional counterpart of the Nyquist frequency. The widely used Cartesian lattice is the reciprocal of itself. While in 2-D, the hexagonal lattice is also reciprocal to itself (rotated by 30 degrees), in 3-D the BCC and FCC lattices are reciprocal to each other (up to scaling). The superiority of sphere-packing (e.g., FCC) and sphere-covering (e.g., BCC) lattices for representing multi-dimensional signals has been studied in sampling theory [26], [27].

In 2-D, the reciprocal to the hexagonal lattice allows for tightest 2-D packing of discs [26]. When compared to the commonly-used Cartesian lattice with the same sampling density, the hexagonal lattice could capture about 14% more information from the spectrum of the underlying signal. This idea has been explored for k-space sampling in MRI [28]. This is illustrated in Figure 1 as the area of the inscribing disc to the Brillouin zone of the hexagonal lattice (i.e., hexagon) which is larger than the area of inscribing disc to the Brillouin zone of the Cartesian lattice (i.e., square), while the two Brillouin zones have unit area.

In 3-D, the optimal lattice is the BCC lattice whose reciprocal lattice (i.e., the FCC lattice) is the densest sphere packing lattice. When discretizing the  $\mathbf{q}$ -space signal  $E(\mathbf{q})$  on a BCC lattice, the spectrum of the signal,  $P(\mathbf{r})$ , is contained in rhombic dodecahedral voxels, which admit a larger inscribing sphere than their Cartesian counterparts. The inscribing sphere to the rhombic dodecahedral voxel is about 30% larger than that of the cubic voxel while the two voxels are both of unit volume. The larger inscribing sphere of the rhombic dodecahedral voxel means that we can preserve 30% extra information about  $P(\mathbf{r})$  without any overlap from the periodic replication which is caused by  $\mathbf{q}$ -space sampling. Therefore, when reconstructing  $P(\mathbf{r})$  on each individual voxel, a reconstruction based on BCC sampling of  $\mathbf{q}$ -space yields greater resolution in  $\mathbf{r}$ , while preventing ghosting artifacts.

### III. Interlaced Sampling Scheme

In diffusion weighted MRI, the diffusion properties of a tissue are determined by measuring its response to an oriented magnetic field gradient. By applying gradients of different strengths and directions, we obtain samples of the diffusion signal in 3-D  $\mathbf{q}$ -space for each voxel location within the tissue. For each  $\mathbf{q}$ -space sample, we need to alter the orientation and/or strength of the magnetic field gradient and measure the response for the entire volume,  $\mathbf{q}$ -space sampling cannot be performed in parallel - the sampling time increases linearly with the number of  $\mathbf{q}$ -space samples. Therefore, within our acquisitions, we seek an optimal balance between the number of samples and reconstruction accuracy.

The sampling scheme determines how the sample points are distributed throughout 3-D  $\mathbf{q}$ -space. An approach, employed by DSI, is to put the samples on a regular Cartesian lattice. This is the most conventional scheme used in signal processing where Shannon sampling theory provides the theoretical framework for sampling and reconstruction. In addition,  $P(\mathbf{r})$  can be reconstructed through the Fast Fourier transform (FFT). However, this scheme is time consuming since it needs a large number of  $\mathbf{q}$ -space samples to achieve a reasonably accurate reconstruction.

In practice, the most widely used sampling scheme in diffusion MR is to take a sample at the origin together with uniformly distributed samples on a spherical shell in the  $\mathbf{q}$ -space. All of the samples on the spherical shell  $|\mathbf{q}| = \sqrt{b/t}/2\pi$  are taken under an applied magnetic field gradient of the same strength but with different directions. The benefit is that variations in signal to noise ratio and other factors related to the strength of the magnetic field are minimized. With some global or directional decay models of the signal,  $P(\mathbf{r})$  can be computed analytically through the continuous Fourier transform [6], [7]. A notable variation of this scheme acquires samples from multiple shells, i.e. multiple  $b$  values, each with the same directional distribution of samples. In this *multi-shell setting*, more sophisticated models involving more parameters can be used. This type of model-based scheme needs fewer samples than DSI and can produce smooth reconstructions, but it is limited by the assumptions of proposed models [6], [7].

In this work, we propose an interlaced sampling scheme as an alternative to the standard multi-shell sampling scheme. The idea of interlaced lattice comes from the structure of the BCC lattice as it can be viewed as a stack of 2-D Cartesian layers of points where every alternate layer is shifted by half of the sampling distance (Figure 2 (c)). In the multi-shell sampling, the proposed interlaced lattice has the interleaving structure in the spherical coordinates where every alternate shell is shifted by half of the angular resolution. A similar idea in 2-D interlaced sampling has been explored for computed tomography [29] which compared the performance of an interlaced sampling scheme with the standard scheme in the case of 2-D computed tomography (CT) reconstruction. For their interlaced scheme, the detector array was shifted by one half of a detector spacing when going from one projection direction to the next. With some good experimental results, this work concluded that the interlaced scheme allows almost twice the resolution of the standard scheme with the same number of samples in 2-D. Figure 2 (a) and (b) shows the sample distributions of both schemes. In the interlaced scheme, samples on the odd and even circles form two different polygons. These two polygons are a pair of dual polygons where the vertices of one correspond to the edges of the other.

By extending the idea of dual polygons to dual polyhedra (the vertices of one correspond to the *faces* of the other), we produced a three-dimensional interlaced sampling scheme. To ensure that samples are uniformly distributed on each spherical shell, one could use the sampling directions defined by the vertices of the commonly-used icosahedron (Figure 3(a))

and its dual, the dodecahedron (Figure 3(b)), alternately for odd and even shells. Icosahedron and dodecahedron are both Platonic solids, i.e. convex regular polyhedrons, which are highly symmetrical, being edge-transitive, vertex-transitive and face-transitive. This property makes them suitable choices as the generators of sampling directions. However, the dodecahedron has 20 vertices while the icosahedron has 12. Therefore, an interlaced sampling scheme based on these two polyhedra would have either greater or fewer samples than a standard multi-shell scheme of comparable sample size. This imbalance makes the comparison of the two approaches difficult.

For a fairer comparison, we used an interlaced scheme based on another pair of dual polyhedra: the rhombic triacontahedron (Figure 3(c)) and icosidodecahedron (Figure 3(d)) who have about the same number of vertices (32 and 30). The vertex directions of the rhombic triacontahedron and icosidodecahedron determined the sampling directions for odd and even shells, respectively. In the standard scheme, all shells were sampled using the vertex directions of the rhombic triacontahedron. Since a rhombic triacontahedron has 32 vertices and the icosidodecahedron has only 30, the interlaced scheme uses slightly fewer samples than the standard scheme. In the experiments section we will see that, even with fewer samples, the interlaced scheme achieves better reconstruction accuracy. If necessary, more sampling directions can be added by subdividing the edges of both polyhedra.

#### IV. Reconstruction Algorithm

In Section III, we proposed the use of an interlaced multi-shell sampling scheme to sample the diffusion signal in  $\mathbf{q}$ -space. This is not an uniform sampling scheme, so we cannot estimate the diffusion propagator directly through FFT. One solution is to estimate the values of  $P(\mathbf{r})$  by numerically computing the integral in (1). However, the irregular distribution of sampling positions makes it difficult to design an accurate numerical integration algorithm. Another solution is to define a regular lattice in  $\mathbf{q}$ -space and estimate the values on this regular lattice through interpolation/extrapolation. In other words, we can resample the diffusion signal on a regular lattice using the nonuniformly sampled values.

Shannon's sampling theory provides a reconstruction formula for a bandlimited function,  $f$ , from its samples on a uniform lattice,  $\mathcal{L}$ , when the sampling rate is higher than the Nyquist frequency of  $f$ :

$$f(\mathbf{x}) = \sum_{\mathbf{x}_k \in \mathcal{L}} f(\mathbf{x}_k) \text{sinc}_{\mathcal{L}}(\mathbf{x} - \mathbf{x}_k) \quad (2)$$

$\text{sinc}_{\mathcal{L}}(\mathbf{x})$  is the ideal interpolation function that depends on the sampling lattice  $\mathcal{L}$ . In the 3-D Cartesian lattice case,  $\text{sinc}_{\mathcal{L}}(\mathbf{x}) = \text{sinc}(x) \text{sinc}(y) \text{sinc}(z)$  where  $\text{sinc}(x) = \frac{\sin(\pi x)}{\pi x}$  is the 1-D sinc function.

For the BCC lattice, the corresponding  $\text{sinc}_{\mathcal{L}}$  is computed, similarly, from the inverse Fourier transform of the indicator function of its Brillouin zone – a rhombic dodecahedron shown in Figure 1. This function can be efficiently evaluated using a geometric approach [24]. The explicit formula for BCC lattice's sinc function is given by:

$$\text{sinc}_{\mathcal{L}}(\mathbf{x}) = \frac{1}{4} \sum_{k=1}^4 \left[ \cos(\pi \xi_k^T \mathbf{x}) \prod_{m \neq k} \text{sinc}(\xi_m^T \mathbf{x}) \right] \quad (3)$$

where

$$[\xi_1 \cdots \xi_4] = \frac{1}{4} \begin{bmatrix} 1 & -1 & -1 & 1 \\ -1 & 1 & -1 & 1 \\ -1 & -1 & 1 & 1 \end{bmatrix}. \quad (4)$$

Shannon's reconstruction formula (e.g., (2)) involves infinitely many terms, which make its evaluation impractical. In practice, only finite terms involving lattice points,  $\mathbf{x}_k$ , within a bounding box are considered non-zero. While only finite terms are considered in the summation, the linear combination of  $\text{sinc}_{\mathcal{L}}$  shifted to these finite lattice points provides an infinitely-supported approximation to  $f$ :

$$\widehat{f}(\mathbf{x}) = \sum_{\mathbf{x}_k \in \mathcal{L}, 1 \leq k \leq K} f(\mathbf{x}_k) \text{sinc}_{\mathcal{L}}(\mathbf{x} - \mathbf{x}_k). \quad (5)$$

The Fourier transform of this approximation has a compact support which will approximate  $P(\mathbf{r})$  in our setting. In our case, the signal under investigation is the diffusion signal  $E(\mathbf{q})$  in  $\mathbf{q}$ -space. We are given  $N$  sample measurements  $E(\mathbf{q}_n)$  on multiple spherical shells, depicted by copper and purple vertices in Figure 4 (a) and Figure 4 (b). The desired estimates are  $K$  values  $E(\mathbf{x}_k)$  on a regular lattice  $\mathbf{x}_k \in \mathcal{L}$ , depicted by gray dots in Figure 4 (a) and Figure 4 (b) for the Cartesian case. The diffusion signal can be approximated according to equation (5) as  $\widehat{E}(\mathbf{q})$ . By matching  $\widehat{E}(\mathbf{q})$  to the measurements  $E(\mathbf{q}_n)$  at locations  $\mathbf{q}_n$ , we get:

$$E(\mathbf{q}_n) = \sum_{\mathbf{x}_k \in \mathcal{L}, 1 \leq k \leq K} E(\mathbf{x}_k) \text{sinc}_{\mathcal{L}}(\mathbf{q}_n - \mathbf{x}_k), n=1, \dots, N \quad (6)$$

where  $N$  is the total number of measurements of  $E(\mathbf{q})$ . Considering  $E(\mathbf{x}_k)$  as unknowns, (6) are  $N$  equations in  $K$  unknowns which can be written as a linear system  $\mathbf{A}\mathbf{e} = \mathbf{b}$ , where  $\mathbf{A}_{n,k} = \text{sinc}_{\mathcal{L}}(\mathbf{q}_n - \mathbf{x}_k)$ ,  $\mathbf{e}_k = E(\mathbf{x}_k)$  and  $\mathbf{b}_n = E(\mathbf{q}_n)$ .

For accurate lattice-based reconstruction, the regular lattice should be dense, so we usually have  $K > N$ .  $K > N$  means that the number of  $\mathbf{q}$ -space measurements is higher than the lattice resolution that we are reconstructing onto. Since the acquisition time is determined by  $N$ , a high sampling rate (e.g., DSI) is impractical. Therefore, we consider  $K > N$  that our reconstruction lattice more dense compared to the acquired sampling rate. This means that (6) is an underdetermined linear system which can be solved in the least-squares sense using normal equations and the conjugate gradient method. To expedite the process, we provide an initial estimate of  $E(\mathbf{x}_k)$  using linear interpolation on a Delaunay triangulation of a set of sample points  $\mathbf{q}_n$ ,  $n = 1, 2, \dots, N$ . One can also obtain solutions with different properties by using different regularizers. For example, using  $L_1$  regularization on some transform coefficients leads to sparse reconstructions as discussed in [30], [31].

Once the signal  $E(\mathbf{q}_n)$  has been estimated on a regular lattice, we get a continuous representation of  $E(\mathbf{q})$  as:

$$E(\mathbf{q}) = \sum_{\mathbf{x}_k \in \mathcal{L}, 1 \leq k \leq K} E(\mathbf{x}_k) \text{sinc}_{\mathcal{L}}(\mathbf{q} - \mathbf{x}_k) \quad (7)$$

Taking Fourier transform on (7), we get:

$$P(\mathbf{r}) = \text{box}(\mathbf{r}) \sum_{\mathbf{x}_k \in \mathcal{L}, 1 \leq k \leq K} E(\mathbf{x}_k) \exp(-2\pi i \mathbf{x}_k \cdot \mathbf{r}) \quad (8)$$

where  $\text{box}(\mathbf{r})$  is the Fourier transform of  $\text{sinc}_{\mathcal{L}}(\mathbf{q})$  which is an indicator function whose support is a cube for Cartesian lattice and a rhombic dodecahedron for BCC lattice.

As discussed in Section II, to capture the same amount of information about the function being sampled, the BCC lattice only needs about 70% of the sample points needed for the Cartesian lattice. This property makes the necessary  $K$  value for the BCC lattice 30% smaller than the  $K$  value for the Cartesian lattice. For solving the underdetermined linear system, smaller  $K$  is preferred, because it means that the linear system has a higher rank. This usually translates to smaller uncertainty in the final solution. On the other hand, for a fixed  $K$  value, resampling on a BCC lattice can reveal more details about the real signal by allowing  $P(\mathbf{r})$  reconstructed by a larger radius while avoiding the ghosting effects[32]. In other words, resampling on a BCC lattice is an effective way of improving the accuracy without increasing the rank of the linear system to be solved.

## V. Experiments

In this section, we present several experimental results on synthetic as well as real data sets. First, the synthetic data examples are presented followed by the real data experiments.

### A. Experiments on synthetic data

In order to show the advantages of our sampling scheme and lattice selection, we first did quantitative comparison using synthetic data. We used a mixture of two oriented Gaussian functions in the 3-D displacement space to simulate the diffusion probability,  $P(\mathbf{r})$ , of a fiber crossing. The two Gaussian functions are the rotated versions of an oriented Gaussian distribution function with zero mean and diagonal covariance matrix  $\mathbf{C} = \text{diag}\{20, 20, 400\}$  which has a fractional anisotropy value of 0.95. These two rotated Gaussian functions are specified by covariance matrices  $\mathbf{C}_1$  and  $\mathbf{C}_2$ .

We fixed one of the Gaussian components and rotate the other component to form crossing angles from  $20^\circ$  to  $60^\circ$  with a  $5^\circ$  step size.

As described earlier,  $\mathbf{q}$ -space data was sampled on multiple shells using both the standard and interlaced schemes. For the standard scheme, the vertex directions of the rhombic triacontahedron defined the sampling directions for all shells. For the interlaced scheme, diffusion directions on even shells were determined from the vertices of the icosidodecahedron. Due to the symmetry of the diffusion signal, i.e.  $\mathcal{S}(\mathbf{q}) = \mathcal{S}(-\mathbf{q})$ , only half of the sampling directions are necessary. Thus, only those directions with  $\mathbf{q}_z \geq 0$  were chosen. The sampling directions are determined by the vertex coordinates of the rhombic triacontahedron and icosidodecahedron.

For the synthetic experiments, we picked 7 different shell radii uniformly distributed between 0 and  $q_{max} = 0.5 \sqrt{1/20}$ . So we had samples on 6 shells plus the origin. The total number of samples was 193 for the standard (non-interlaced) scheme and 187 for the interlaced scheme (symmetric directions included). The data were interpolated onto two embedding lattices: the  $15 \times 15 \times 15$  Cartesian lattice and the equivalent BCC lattice, which consists of two staggered Cartesian lattices of size  $11 \times 11 \times 11$  and  $12 \times 12 \times 12$  respectively. The numbers of lattice points were 3375 for Cartesian and 3059 for BCC respectively.

The reconstructed diffusion propagators,  $P(\mathbf{r})$  at different  $\|\mathbf{r}\|$  values, obtained using different sampling schemes and embedding lattices are shown as Figure 5. We can see that the interlaced sampling scheme has higher angular discrimination than the standard (non-interlaced) scheme. In the interlaced sampling case, the two-fiber crossing geometry is

correctly reconstructed when the crossing angle is greater than or equal to  $35^\circ$ . In the standard case, the crossing geometry is not recovered faithfully for angular separation smaller than  $45^\circ$ . Also, the reconstructions from interlaced scheme are sharper and of higher fidelity with respect to the true geometry of  $P(\mathbf{r})$ . When we compare the reconstructions from Cartesian and BCC embedding lattices, the latter always has less distortion because using a BCC embedding lattice leads to smaller aliasing effects on  $P(\mathbf{r})$ .

In addition to the visual comparison, some numerical comparison of the reconstruction errors is also necessary. In our multi-shell, model-free scenario, mean square error (MSE) of the reconstructed  $\widehat{P}(\mathbf{r})$  compared with the true  $P(\mathbf{r})$  is a good choice because it indicates both radial and angular reconstruction accuracy. According to Plancherel theorem, it is equivalent to the MSE of the reconstructed  $\widehat{E}(\mathbf{q})$  in  $\mathbf{q}$ -space. Thus, we use the MSE of  $\widehat{E}(\mathbf{q})$  on the embedding lattice points as our error measurement. This error is further divided by the mean value of the true  $E^2(\mathbf{q})$  as a normalization so that it is not dependent on the magnitude of the signal. We repeated the reconstruction procedure with varying amounts of Rician noise,  $\delta_r$ . The results are shown in Figure 6. It is evident that the interlaced scheme gives less error than the standard scheme and the BCC embedding lattice even further reduces the error. The benefit of BCC lattice over Cartesian lattice is rooted in its ability to capture extra high frequency information without introducing aliasing. But when this information is too noisy, the benefits gradually disappear. As such, the reconstruction errors using Cartesian and BCC lattices approach each other when the noise level increases.

We have shown the visual and numerical comparison of different reconstruction schemes on 2-fiber crossing synthetic data. To explore different fiber configurations, we repeat the comparison on 3-fiber synthetic data. The visual comparisons are depicted in Figure 7. The numerical comparisons are shown in Figure 8. In the end, we all also verified that our proposed scheme outperforms the standard (non-interlaced) scheme for different FA values of 0 and 0.6.

## B. Experiments on real data

To further test our scheme, we acquired real MRI data using both the standard and interlaced multi-shell sampling schemes and compared the reconstruction results. All magnetic resonance imaging was performed on a 600MHz (14.1 Tesla) Bruker imaging spectrometer, using a conventional diffusion weighted spin echo pulse sequence. The sampling directions are the same as those used for the synthetic experiments. Three multi-shell datasets, which captured different regions of the mouse brain were acquired: 1) a coronal set at the level of the corpus callosum, 2) a coronal set through the brain stem at the level of the superior colliculus, and 3) a sagittal set through the midline. All the datasets were pre-processed with non-local means filtering to reduce the noise [33], [34].

Dataset #1 was acquired with: slice thickness =  $0.7\text{mm}$ ,  $1.2 \times 1.2\text{cm}^2$  field-of-view,  $128 \times 128$  data matrix, and  $94\mu\text{m}$  in-plane resolution. Diffusion parameters included: diffusion time,  $\Delta = 15\text{msec}$ , diffusion gradient duration,  $\delta = 1\text{msec}$ , and b-values of 500, 1000, 2000, 3000, 4000 and 5000  $\text{s/mm}^2$  ( $\|\mathbf{q}\| = 29.1, 41.1, 58.1, 71.2, 82.2, \text{ and } 91.9 \text{ mm}^{-1}$ ).

Dataset #2 was acquired with: slice thickness =  $0.3\text{mm}$ ,  $1.2 \times 1.2\text{cm}^2$  field-of-view,  $192 \times 192$  data matrix,  $62.5\mu\text{m}$  in-plane resolution,  $\Delta = 12\text{msec}$ ,  $\delta = 1\text{msec}$ , and b-values of 187, 750, 1687, and 3000  $\text{s/mm}^2$ . The nonuniform spacing between b-values was chosen to provide roughly equal spacing between  $q$ -values ( $\|\mathbf{q}\| = 20.2, 40.3, 60.5, \text{ and } 80.7 \text{ mm}^{-1}$ ).

Dataset #3 was acquired with: slice thickness =  $0.35\text{mm}$ ,  $1.8 \times 0.9\text{cm}^2$  field-of-view,  $256 \times 128$  data matrix, and  $70.3\mu\text{m}$  in-plane resolution. Diffusion parameters were identical to those used for dataset #2.

The choice of maximum  $b$  (or  $\|\mathbf{q}\|$ ) is a compromise between signal-to-noise ratio (SNR) and resolution of the diffusion propagator,  $P(\mathbf{r})$ . In the experimental data, the SNR of the highest  $b$ -value image was 15, 16 and 25 for datasets 1, 2, and 3, respectively. SNR was computed from magnitude images, by dividing the mean of the signal over the entire object by the standard deviation of the noise in an artifact-free background region. The values provided represent the minimum across all of the sampled diffusion directions.

Further increases in  $\|\mathbf{q}\|$  or  $b$  were avoided to limit the Rician noise bias within the data [7]. This comes at the expense of  $P(\mathbf{r})$  resolution, which is equal to the inverse of the maximal  $\mathbf{q}$ -value [4]. While additional resolution is desirable, acquiring noisy data at high  $\mathbf{q}$ - (or  $b$ -) values may not represent an efficient use of the available imaging time. Instead, more time was spent on higher SNR acquisitions at intermediate  $b$ -values. This allows for finer sampling of the diffusion signal,  $E(\mathbf{q})$ , which reduces aliasing distortion in  $P(\mathbf{r})$ . The total imaging time for the experimental data acquired with the standard sampling scheme was approximately 34, 35 and 28 hours for datasets 1, 2, and 3 respectively. The interlaced scheme decreases the total scan time by roughly an hour.

Figure 9 shows the reconstruction results of dataset #1. The boxed region of interest contains intersecting fiber bundles from cingulum and corpus callosum. Our proposed scheme provides sharper reconstructions of the fiber crossings in the identified ROI. Figure 10 shows the reconstruction results of dataset #2. We picked this region of interest because it has been validated that there are plenty of in-plane crossing fibers in this region [35]. The results show that our proposed scheme can recover the crossings more accurately. Figure 11 shows the reconstruction results of dataset #3. The branching structure in the highlighted region of interest is obvious. Our proposed scheme provides sharper reconstructions of those fiber crossings.

The comparisons of the reconstructed diffusion propagators using 4 different settings, standard or interlaced scheme with Cartesian or BCC lattice, are shown in Figure 9, Figure 10 and Figure 11 as (d), (e), (f) and (g). The interlaced scheme with BCC lattice is the clear winner in its ability to accurately reconstruct sharp crossings.

## VI. Conclusion

This paper proposes a new framework for the estimation of the diffusion propagator, which includes a novel interlaced sampling scheme and a model-free reconstruction using optimal lattices. This framework boosts the accuracy of the reconstructed diffusion propagator in two ways: 1) the interlaced multi-shell sampling scheme increases the angular discrimination in  $\mathbf{q}$ -space without increasing the acquisition time; 2) the technique is model-free – it resamples the multi-shell data onto a regular lattice and obtains  $P(\mathbf{r})$  using the FFT. Resampling to a BCC (rather than the commonly-used Cartesian) lattice further increases the reconstruction accuracy due to the smaller ghosting effects of the dual FCC lattice. Another direction that the proposed framework can be applied is for the reduction of acquisition time, compared to the standard (non-interlaced) data acquisition scheme, where we can achieve the same reconstruction accuracy, with fewer samples. We have provided evidence for the advantages of the proposed framework via the analysis of simulated and experimental data.

## Acknowledgments

Entezari was supported in part by the NSF grant CCF-1018149, Vemuri by the NIH grant NS066340 and Ye by the grants NIH NS066340 and NSF CCF-1018149 respectively.

## References

- [1]. Moseley M, Cohen Y, Mintorovitch J, Chileuitt L, Shimizu H, Kucharczyk J, Wendland M, Weinstein P. Early detection of regional cerebral ischemia in cats: comparison of diffusion- and T2-weighted MRI and spectroscopy. *Magnetic Resonance in Medicine*. 1990; 14(2):330–346. [PubMed: 2345513]
- [2]. Tuch D, Reese T, Wiegell M, Van J W. Diffusion MRI of complex neural architecture. *Neuron*. 2003; 40(5):885–895. [PubMed: 14659088]
- [3]. Aganj I, Lenglet C, Sapiro G, Yacoub E, Ugurbil K, Harel N. Reconstruction of the orientation distribution function in single- and multiple-shell q-ball imaging within constant solid angle. *Magnetic Resonance in Medicine*. 2010; 64(2):554–566. [PubMed: 20535807]
- [4]. Cohen Y, Assaf Y. High b-value q-space analyzed diffusion-weighted MRS and MRI in neuronal tissues—a technical review. *NMR in Biomedicine*. 2002; 15(7–8):516–542. [PubMed: 12489099]
- [5]. Callaghan, P. *Principles of Nuclear Magnetic Resonance Microscopy*. Clarendon Press; Oxford: 1991.
- [6]. Jian B, Vemuri B, Ozarslan E, Carney P, Mareci T. A novel tensor distribution model for the diffusion-weighted MR signal. *NeuroImage*. 2007; 37(1):164–176. [PubMed: 17570683]
- [7]. Descoteaux M, Deriche R, Le Bihan D, Mangin J, Poupon C. Multiple q-shell diffusion propagator imaging. *Medical Image Analysis*. 2011; 15:603–621. [PubMed: 20685153]
- [8]. Basser PJ, Mattiello J, LeBihan D. MR diffusion tensor spectroscopy and imaging. *Biophysical J*. 1994; 66:259–267.
- [9]. Barmoutis A, Hwang M, Howland D, Forder J, Vemuri BC. Regularized positive-definite fourth-order tensor field estimation from dw-mri. *NeuroImage*. 2009; 45(1):153–162.
- [10]. Özarlan E, Shepherd TM, Vemuri BC, Blackband SJ, Mareci TH. Resolution of complex tissue microarchitecture using the diffusion orientation transform (DOT). *NeuroImage*. 2006; 31:1086–1103. [PubMed: 16546404]
- [11]. Tristán-Vega A, Westin C, Aja-Fernández S. Estimation of fiber orientation probability density functions in high angular resolution diffusion imaging. *NeuroImage*. 2009; 47(2):638–650. [PubMed: 19393321]
- [12]. Frank L. Characterization of anisotropy in high angular resolution diffusion weighted MRI. *Magnetic Resonance in Medicine*. 2002; 47(6):1083–1099. [PubMed: 12111955]
- [13]. Alexander DC, Barker GJ, Arridge SR. Detection and modeling of non-Gaussian apparent diffusion coefficient profiles in human brain data. *Magnetic Resonance in Medicine*. Aug; 2002 48(2):331–340. [PubMed: 12210942]
- [14]. Özarlan E, Mareci TH. Generalized DTI and analytical relationships between DTI and HARDI. *Magnetic Resonance in Medicine*. 2003; 50(5):955–965. [PubMed: 14587006]
- [15]. Assaf Y, Freidlin R, Rohde G, Basser P. New modeling and experimental framework to characterize hindered and restricted water diffusion in brain white matter. *Magnetic Resonance in Medicine*. 2004; 52(5):965–978. [PubMed: 15508168]
- [16]. Tournier J, Calamante F, Gadian D, Connelly A. Direct estimation of the fiber orientation density function from diffusion-weighted MRI data using spherical deconvolution. *NeuroImage*. 2004; 23(3):1176–1185. [PubMed: 15528117]
- [17]. Ozarslan, E.; Koay, C.; Shepherd, T.; Blackband, S.; Basser, P. ISMRM. 2009. Simple harmonic oscillator based reconstruction and estimation for three-dimensional q-space MRI; p. 1396
- [18]. Cheng J, Ghosh A, Jiang T, Deriche R. Model-free and analytical EAP reconstruction via spherical polar fourier diffusion MRI. *MICCAI*. 2010:590–597. [PubMed: 20879279]
- [19]. Chiang, W.; Wedeen, V.; Kuo, L.; Perng, M.; Tseng, W. ISMRM. 2006. Diffusion spectrum imaging using body-center-cubic sampling scheme; p. 1041

- [20]. Pickalov, V.; Basser, P. ISBI. 2006. 3d tomographic reconstruction of the average propagator from mri data; p. 710-713.
- [21]. Wu Y, Alexander A. Hybrid diffusion imaging. *NeuroImage*. 2007; 36(3):617–629. [PubMed: 17481920]
- [22]. Assaf Y, Basser P. Composite hindered and restricted model of diffusion (CHARMED) MR imaging of the human brain. *NeuroImage*. 2005; 27(1):48–58. [PubMed: 15979342]
- [23]. Assemlal, H-E.; Tschumperlé, D.; Brun, L. MICCAI. London/England: Sep. 2009 Evaluation of q-space sampling strategies for the diffusion magnetic resonance imaging; p. 406-414.
- [24]. Ye W, Entezari A. A geometric construction of multivariate Sinc functions. *IEEE Transactions on Image Processing*. 2011 Accepted.
- [25]. Dudgeon, DE.; Mersereau, RM. *Multidimensional Digital Signal Processing*. 1st ed.. Prentice-Hall, Inc.; Englewood-Cliffs, NJ: 1984.
- [26]. Petersen DP, Middleton D. Sampling and reconstruction of wave-number-limited functions in  $N$ -dimensional Euclidean spaces. *Information and Control*. 1962; 5(4):279–323.
- [27]. Kunsch H, Agrell E, Hamprecht F. Optimal lattices for sampling. *IEEE Trans. on Information Theory*. 2005; 51(2):634–647.
- [28]. Ehrhardt JC. MR Data Acquisition and Reconstruction Using Efficient Sampling Schemes. *IEEE Transactions on Medical Imaging*. Sep; 1990 9(3):305–309. [PubMed: 18222777]
- [29]. Faridani A, Ritman E. High-resolution computed tomography from efficient sampling. *Inverse Problems*. 2000; 16:635.
- [30]. Menzel M, Tan E, Khare K, Sperl J, King K, Tao X, Hardy C, Marinelli L. Accelerated diffusion spectrum imaging in the human brain using compressed sensing. *Mag. Res. in Medicine*. 2011; 66(5):1226–1233.
- [31]. Cheng, J.; Merlet, S.; Caruyer, E.; Ghosh, A.; Jiang, T.; Deriche, R. MICCAI Workshop on CDMRI. Toronto, Canada: 2011. Compressive Sensing Ensemble Average Propagator Estimation via L1 Spherical Polar Fourier Imaging.
- [32]. Ye, W.; Entezari, A.; Vemuri, BC. ISBI. 2010. Tomographic reconstruction of diffusion propagators from DW-MRI using optimal sampling lattices; p. 788-791.
- [33]. Coupé P, Yger P, Prima S, Hellier P, Kervrann C, Barillot C. An optimized blockwise nonlocal means denoising filter for 3-D magnetic resonance images. *IEEE Transactions on Medical Imaging*. 2008; 27(4):425–441. [PubMed: 18390341]
- [34]. Descoteaux M, Wiest-Daesslé N, Prima S, Barillot C, Deriche R. Impact of rician adapted non-local means filtering on hardi. *MICCAI*. 2008:122–130. [PubMed: 18982597]
- [35]. Leergaard T, White N, De Crespigny A, Bolstad I, DArceuil H, Bjaalie J, Dale A. Quantitative histological validation of diffusion MRI fiber orientation distributions in the rat brain. *PLoS One*. 2010; 5

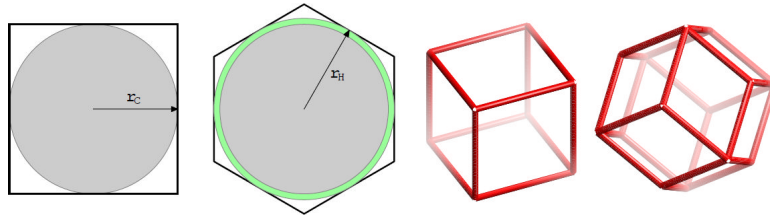


**Fig. 1.**

A square and a hexagonal pixel with unit area correspond to Brillouin zones of Cartesian and hexagonal sampling in  $\mathbf{q}$ -space. The area of inscribing disc for a square is about 14% less than the area of the inscribing disc for the hexagon. In 3-D, this difference is about 30%, comparing a cubic voxel to rhombic-dodecahedron, the voxel of the FCC lattice, with the same volume.

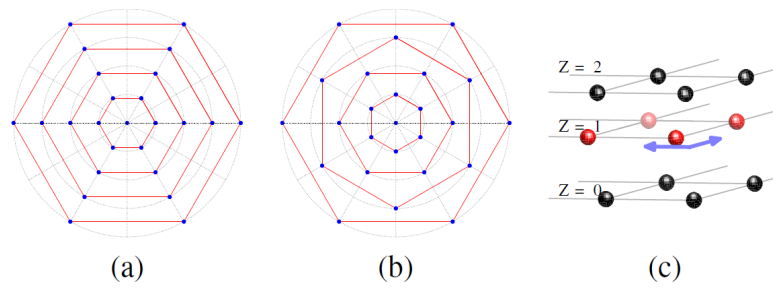


**Fig. 2.** (a) Standard radial sampling scheme, (b) interlaced sampling scheme, (c) the structure of BCC lattice as 2-D Cartesian layers of samples *shifted* on alternate  $Z$  slices.

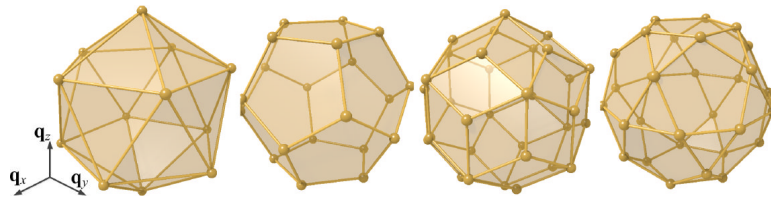


**Fig. 3.** Shape of polyhedra used in this paper. From left to right: Icosahedron, 12 vertices, 30 edges, 20 faces, Dodecahedron, 20 vertices, 30 edges, 12 faces, Rhombic triacontahedron, 32 vertices, 60 edges, 30 faces, Icosidodecahedron, 30 vertices, 60 edges, 32 faces.

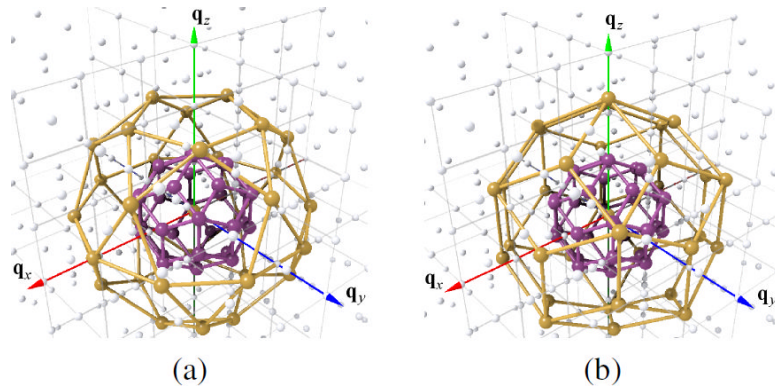


**Fig. 4.** (a) Interlaced multi-shell sampling directions defined on rhombic triacontahedron (purple) and icosidodecahedron (copper) in an alternative manner. (b) Standard multi-shell sampling directions defined on rhombic triacontahedron over all the shells. Rhombic triacontahedron has 32 vertices, 60 edges and 30 faces. Icosidodecahedron has 30 vertices, 60 edges and 32 faces.

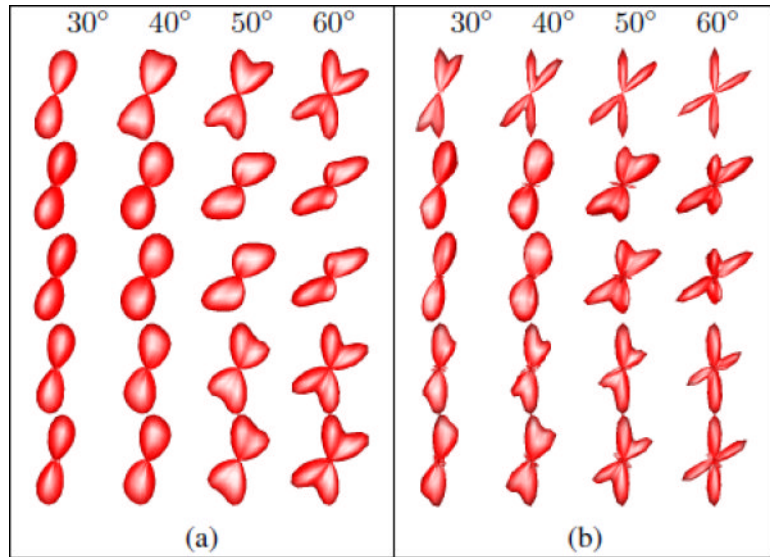


**Fig. 5.** Reconstruction of  $P(\mathbf{r})$  in the two-fiber case, evaluated at (a)  $\|\mathbf{r}\| = 15$  and (b)  $\|\mathbf{r}\| = 25$ , using different sampling scheme and embedding lattices. In each figure, we have: first row: true values of  $P(\mathbf{r})$ , second row: reconstructions using standard scheme and Cartesian lattice, third row: using standard scheme and BCC lattice, forth row: using interlaced scheme and Cartesian lattice, fifth row: using interlaced scheme and BCC lattice.

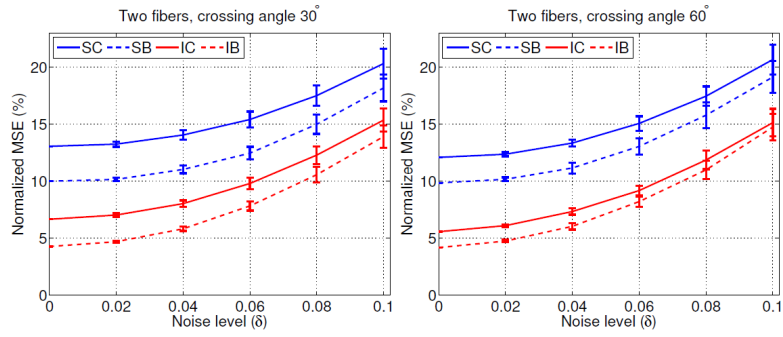


**Fig. 6.** The normalized MSE of the reconstruction for synthetic data of two-fiber crossings. In the legend, SC: standard scheme with Cartesian lattice. SB: standard scheme with BCC lattice. IC: interlaced scheme with Cartesian lattice. IB: interlaced scheme with BCC lattice.

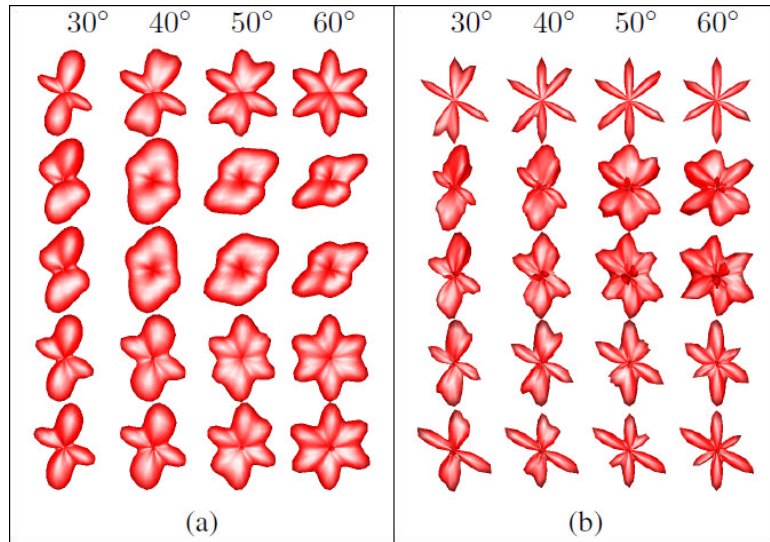


**Fig. 7.** Reconstruction of  $P(\mathbf{r})$  in the three-fiber case, evaluated at (a)  $\|\mathbf{r}\| = 10$  and (b)  $\|\mathbf{r}\| = 15$ . Two fixed fibers are of  $120^\circ$  crossing and the third fiber is rotating to form different angle to the vertical fiber. The arrangement of the figure is the same as Figure 5.

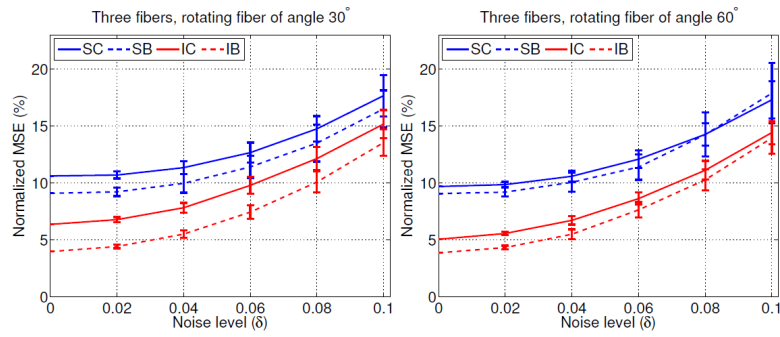


**Fig. 8.** The normalized MSE of the reconstruction for synthetic data of three-fiber crossings.

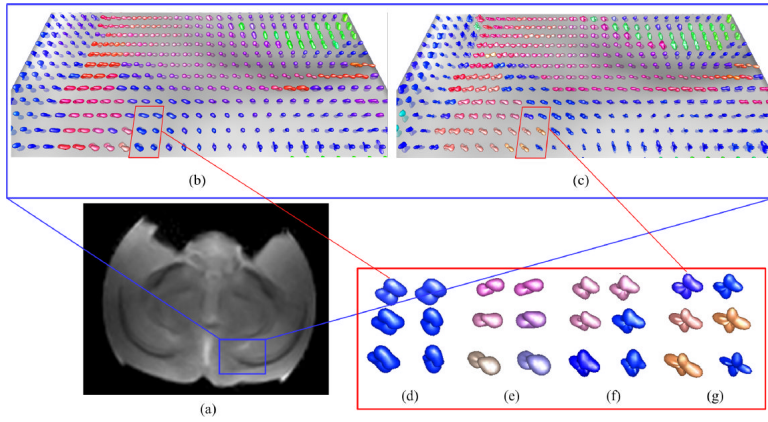


**Fig. 9.** Reconstruction results on dataset #1 evaluated at  $\|\mathbf{r}\| = 8.0\mu\text{m}$ . (a)  $S_0$  image where the region of interest (ROI) is shown in the blue box. Reconstruction using (b) non-interlaced scheme and Cartesian lattice, (c) the proposed interlaced scheme and BCC lattice. Zoom-in views of reconstructions on several voxels using standard scheme with Cartesian lattice (SC) (d), standard scheme with BCC lattice (SB) (e), interlaced scheme with Cartesian lattice (IC) (f), interlaced scheme with BCC lattice (IB) (g).

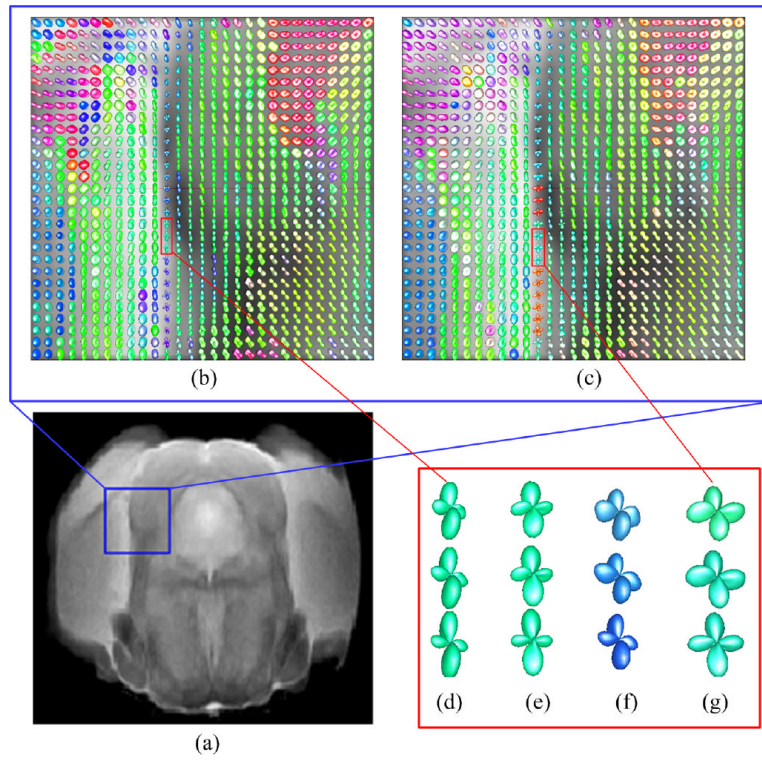


**Fig. 10.** Reconstruction of dataset #2 evaluated at  $\|\mathbf{r}\| = 9.8\mu\text{m}$ . The arrangement of the figure is the same as Figure 9.

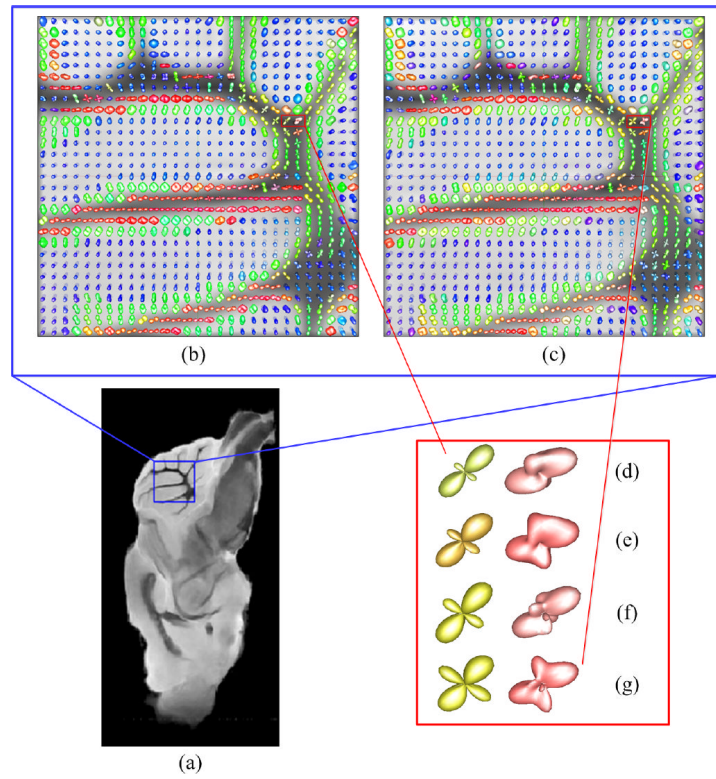


**Fig. 11.** Reconstruction of dataset #3 evaluated at  $\|\mathbf{r}\| = 10.0\mu\text{m}$ . The arrangement of the figure is the same as Figure 9.